mater.scichina.com link.springer.com

Published online 30 September 2021 | https://doi.org/10.1007/s40843-021-1780-x
Sci China Mater 2022, 65(3): 646–652

Achieving superior high-temperature sodium storage performance in a layered potassium vanadate

Dong Chen[1†], Yafei Cheng[2†], Hongge Pan[3,4], Wenping Sun[3,4], Hongbo Geng[2*] and Xianhong Rui[1*]

ABSTRACT **The high-temperature sodium-ion batteries (SIBs) used for large-scale energy storage have attracted extensive attention in recent years. However, the development of SIBs is still hampered mainly by their poor charge/discharge efficiency and stability, necessitating the search for appropriate electrodes. A simple potassium ion intercalation process is used herein to obtain the potassium vanadate (KV_3O_8) nanobelts. When serving as the anode for SIBs at a high temperature (60°C), the KV_3O_8 nanobelts display superior sodium storage performance with a high capacity of 414 mA h g^{-1} at 0.1 A g^{-1}, remarkable rate capability (220 mA h g^{-1} at 20 A g^{-1}), and super-long cycle life (almost no capacity fading at 10 A g^{-1} over 1000 cycles). Moreover, the *ex-situ* X-ray powder diffraction reveals no structural changes throughout the whole charge/discharge process, which further confirms their outstanding stability, indicating KV_3O_8 nanobelts are a promising candidate for high-temperature SIBs.**

Keywords: sodium-ion battery, high-temperature performance, layered potassium vanadate

INTRODUCTION

In recent years, lithium-ion batteries (LIBs) have demonstrated their importance in powering devices [1–10]. The wide application of LIBs has been severely limited due to the scarcity and uneven geographical distribution of lithium resources [11–20]. Because of the abundant sodium element reserves, low price, and similar physicochemical properties to LIBs, sodium-ion batteries (SIBs) have recently been considered as an important potential energy storage device [21–28]. Unfortunately, the relatively high atomic weight (23 g mol^{-1}, heavier than 6.9 g mol^{-1} of lithium) and large radius of Na^+ (1.02 Å, larger than 0.76 Å of lithium) lead to poor rate performance and severe volume expansion during the electrochemical sodiation/desodiation processes [29–36]. Therefore, searching for excellent electrode materials for developing superior SIBs becomes urgent.

To develop appropriate electrode materials for SIBs, several compounds (including hard carbon [37–39], metals and alloys [40–42], metal oxides [43,44], and metal chalcogenides [45–48]) have been widely studied. Among the reported electrode materials for SIBs, the common MV_3O_8 (M = metal) layered oxides possessing high capacity because of the large interlayer spacing and the redox of V^{3+}/V^{5+} couple, have attracted enormous attention. Among the MV_3O_8 layered oxides, the layer spacing of KV_3O_8, 7.48 Å, is much wider than that of LiV_3O_8 (6.32 Å) and NaV_3O_8 (6.85 Å), which is beneficial to the diffusion of sodium ions [49]. For example, Kim *et al.* [50] fabricated KV_3O_8 rectangular plates *via* a hydrothermal route, which delivered a discharge capacity of 182 mA h g^{-1} at 1.75 A g^{-1}, with excellent stability after 500 cycles as the cathode in rechargeable zinc-ion batteries. Tang *et al.* [49] reported KV_3O_8 nanowires, which showed a reversible capacity of 38 mA h g^{-1} (a current density of 100 mA g^{-1}) as a magnesium ion battery cathode. Despite these attractive features, there are few studies about KV_3O_8 as the anode for high-temperature sodium batteries.

In this work, a cost-effective potassium intercalation process is developed to prepare KV_3O_8 nanobelts. The KV_3O_8, which serves as the high-temperature (60°C) SIB anode, features a high capacity of 414 mA h g^{-1} at a current density of 0.1 A g^{-1}, superior rate performance, and excellent stability. The high ion diffusivity (6.2×10^{-7}–1.9×10^{-9} cm^2 s^{-1}) and reversible (de) intercalation reaction of KV_3O_8 during the charging/discharging process may explain the excellent high-temperature sodium storage performance, making it a promising anode material for high-temperature SIBs.

EXPERIMENTAL SECTION

Materials preparation

Fabrication of KV_3O_8 nanobelts anode: 0.1 mol of KCl was dissolved in 200 mL of deionized water using a sonicator for 30 min, and then 1 g of commercial V_2O_5 powder was added. The above solution was then kept at room temperature for seven days with vigorous stirring. The precipitates were then washed with deionized water and ethanol for several times before being centrifuged. Finally, the KV_3O_8 nanobelts were isolated by drying the precipitates for 12 h at 80°C.

Characterizations

Powder X-ray diffraction (XRD, Bruker D8) was used to study

[1] School of Materials and Energy, Guangdong University of Technology, Guangzhou 510006, China
[2] School of Materials Engineering, Changshu Institute of Technology, Changshu 215500, China
[3] Institute of Science and Technology for New Energy, Xi'an Technological University, Xi'an 710021, China
[4] School of Materials Science and Engineering, State Key Laboratory of Silicon Materials, Zhejiang University, Hangzhou 310027, China
† These authors contributed equally to this work.
* Corresponding authors (emails: xhrui@gdut.edu.cn (Rui X); hbgeng@cslg.edu.cn (Geng H))

the crystal structure. The morphology was investigated by transmission electron microscopy (TEM, JEM-2100F, 200 kV) and scanning electron microscopy (SEM, JSM-7500F, 5 kV). The surface chemical state was analyzed by X-ray photoelectron spectroscopy (XPS, ESCALAB, 250Xi). Thermogravimetric analysis (TGA) was operated on the STA 449C within the range of 30–500°C in an argon atmosphere. Brunauer-Emmett-Teller (BET) test was carried out on an ASAP 2020 Automatic Micropore Physisorption Analyzer.

Electrochemical measurements

The working electrode was prepared by coating active material slurry (containing 80 wt% KV_3O_8, 10 wt% carbon nanotubes, and 10 wt% poly(vinylidenefluoride) (PVDF) in *N*-methylpyrrolidone (NMP)) onto the copper foils and dried under 60°C for 8 h in a vacuum oven. Na foils and 1 mol L^{-1} $NaPF_6$ in 1,2-dimethoxyethane (DME) were used as anodes and electrolytes, respectively. The sodium storage performance was evaluated by using a coin-type cell on a NEWARE multichannel battery test system. The galvanostatic discharge/charge tests were carried out at the voltages of 0.01–2.8 V *versus* Na^+/Na. Electrochemical impedance spectra (EIS) and cyclic voltammetry (CV) were performed on a Gamry electrochemical workstation.

RESULTS AND DISCUSSION

Materials manufacturing

Fig. 1 illustrates the preparation of KV_3O_8 nanobelts by a simple and inexpensive potassium intercalation process. The dissolution and recrystallization of particles, which are an unusual anti-Ostwald ripening behavior, are responsible for the formation of nanobelts [51]. K^+ ions are attached to the distorted VO_6 octahedron of KV_3O_8, as shown in Fig. S1. Two V atoms lay in the VO_5 groups of both cones, which are chained along the *b* axis by relative base angles. These chains are linked laterally to the third V atom along the *c*-axis to generate a sheet and also form the part of the square pyramid coordination (Fig. S1). The interlayer distance of KV_3O_8 increases to 7.48 Å, which is significantly larger than that of the original V_2O_5.

The XRD pattern of the ultrathin KV_3O_8 nanobelts is demonstrated in Fig. 2a. The diffraction peaks are assigned to the monoclinic KV_3O_8 (JCPDS card no. 22-1247), in which four main diffraction peaks of 11.7°, 15.7°, 25.7° and 27.9° correspond to (100), (110), (210), and (021) planes of KV_3O_8, respectively. In addition, the peaks of commercial V_2O_5 can be allocated to the orthorhombic V_2O_5 (JCPDS card no. 41-1426). No impurity peaks are observed, indicating the pure phase of KV_3O_8 and V_2O_5. The TGA analysis was performed to confirm whether there is structural water in KV_3O_8. As illustrated in Fig. S2, the TGA curve of KV_3O_8 reveals no decreasing process from 30 to 500°C, indicating no structural water. XPS was performed to study surface chemical compositions and electronic properties of KV_3O_8. For the V 2p XPS spectrum of KV_3O_8 in Fig. 2b, two peaks appear at 517.3 and 524.9 eV, assigned to the $2p_{3/2}$ and $2p_{1/2}$ components of V^{5+}, respectively, indicating that V^{5+} of KV_3O_8 is not reduced to lower vanadium oxidation states during the potassium intercalation process. The K 2p XPS spectrum of KV_3O_8 in Fig. 2c shows two distinct characteristic peaks at 292.6 and 295.4 eV, which can be assigned to K $2p_{3/2}$ and K $2p_{1/2}$, respectively, demonstrating the existence of potassium ions. The O 1s of KV_3O_8 in Fig. 2d shows the V–O peak at around 530.2 eV [52,53].

Fig. 3a and Fig. S3 show low-magnification SEM images of the KV_3O_8 nanobelts with the length of about 10–50 μm. A close-up view in Fig. 3b displays a single nanobelt. From the TEM image (Fig. 3c), it is clear that the width of the nanobelt is ~200 nm. The spacing was calculated to be 0.24 nm, which corresponds to the (310) plane of monoclinic KV_3O_8 (inset of Fig. 3c). Furthermore, the uneven surface of the nanobelts can increase the contact area with the electrolyte. As can be seen in Fig. S4, the BET surface area of the KV_3O_8 nanobelts was determined to be about 26.1 m^2 g^{-1}. Fig. 3d further indicates the even distribution of V, K, and O elements through the entire nanobelt. To investigate the formation mechanism of KV_3O_8 nanobelts, SEM images were recorded at different times, as shown in Fig. S5. At first, the vanadium pentoxide powder was partially dissolved in KCl solution, which yielded free vanadium-based species such as $[V_{10}O_{28}]^{6-}$ and VO_2^+ [51]. As the reaction progress, the vanadium-based species recrystallized to generate KV_3O_8 nuclei when their concentration came up to sufficiently high. Then, with the continuous deposition of vanadium-based species on KV_3O_8 nuclei, the belt-like structure emerged (Fig. S5b–d). Finally, as time went on, vanadium pentoxide particles dis-

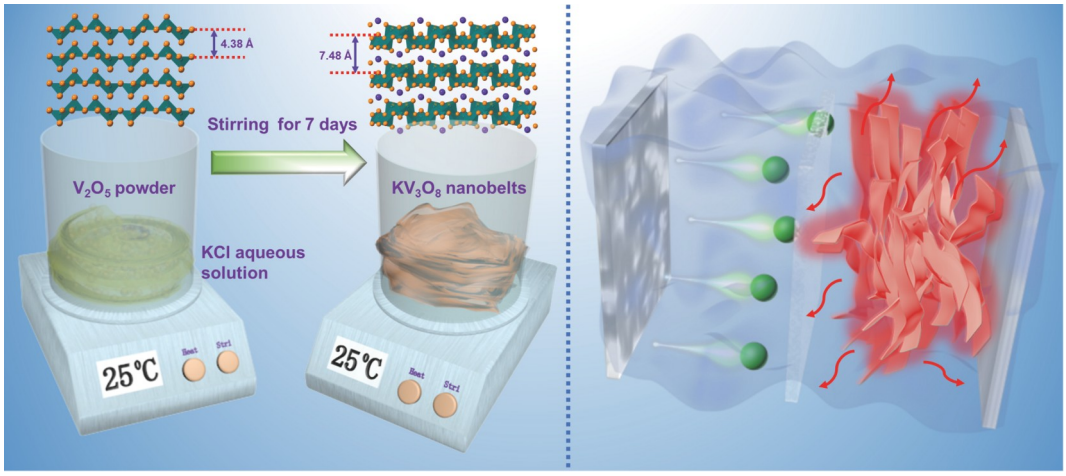

Figure 1 Schematic illustration of the room-temperature synthesis of KV_3O_8 nanobelts.

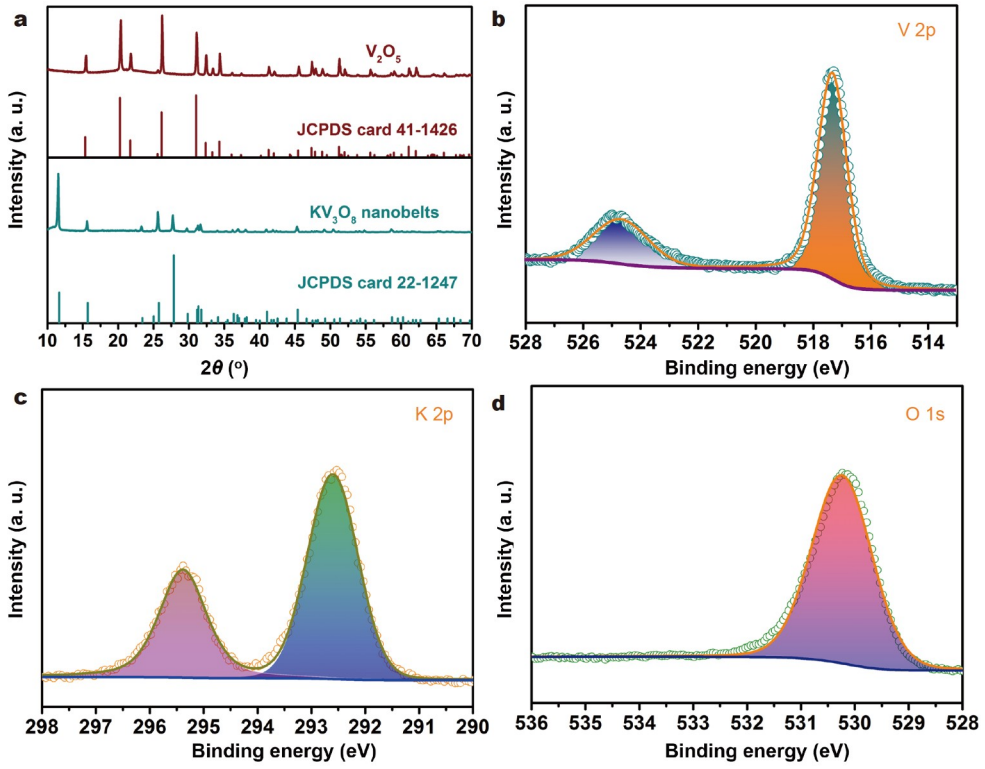

Figure 2 Structure analyses of KV_3O_8. (a) XRD pattern of KV_3O_8. High-resolution XPS spectra of (b) V 2p, (c) K 2p and (d) O 1s.

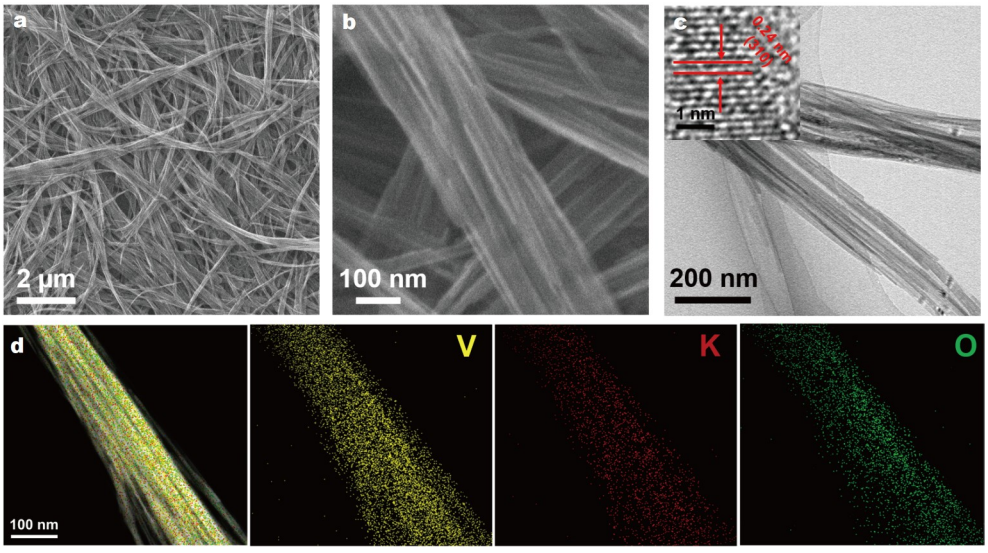

Figure 3 Microstructure and morphology of KV_3O_8. (a, b) SEM images. (c) TEM image and HRTEM image (inset). (d) Scanning TEM (STEM) and the corresponding elemental mapping images.

appeared and KV_3O_8 nanobelts appeared (Fig. S5e).

Electrochemical performance

The sodium storage properties of the KV_3O_8 anodes at high temperatures were investigated by CV and galvanostatic charge/discharge measurements. Fig. 4a illustrates the corresponding CV curves for KV_3O_8 during the initial four cycles at 0.1 mV s^{-1}. Peaks at 1.99, 1.67, 1.29, 0.85, and 0.27 V can be attributed to the sodiation into the KV_3O_8 nanobelts during the first cathodic process, which also forms a solid electrolyte interface layer. Three peaks in the anodic scan correspond to the desodiation from KV_3O_8 nanobelts: 1.56, 1.82, and 2.10 V. The CV curve shows good repeatability after the second cycle, demonstrating the outstanding electrochemical reversibility. When the KV_3O_8 nanobelts are galvanically cycled at 0.1 A g^{-1} (60°C, Fig. 4b), it delivers high capacities (discharge: 688 mA h g^{-1} and charge: 552 mA h g^{-1}). Besides, it achieves a satisfying initial Coulombic efficiency (ICE: 80%). In contrast, the V_2O_5 delivers a low ICE of 66% (Fig. S6). Fig. 4c compares the cycling performance of the KV_3O_8 and V_2O_5 anode at 0.1 A g^{-1} (60°C), in which the KV_3O_8

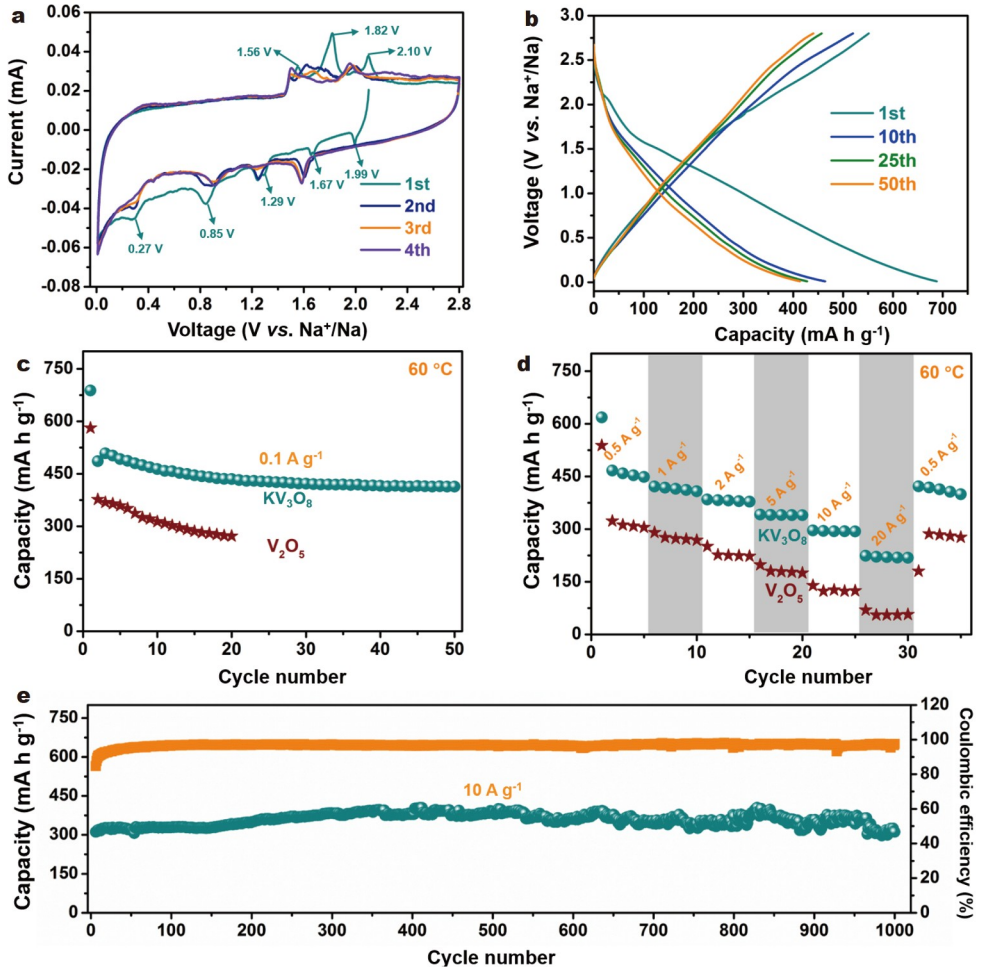

Figure 4 Electrochemical performance of KV_3O_8 anode at 60°C. (a) CV curves. (b) Charge/discharge profiles at 0.1 A g^{-1}. (c) Cycling performance at 0.1 A g^{-1}. (d) Rate performance and (e) long-term cycling performance at 10 A g^{-1}.

anode shows excellent sodium storage capacity, while the V_2O_5 anode exhibits low reversible capacity. Moreover, the high-temperature sodium storage performance of the KV_3O_8 is far better than that of other reported materials (Fig. S7). For example, $NaV_{1.25}Ti_{0.75}O_4$ anode possesses 106 mA h g^{-1} at 0.02 A g^{-1} (60°C) [54], loofah-like NHCNFs (nitrogen-doped hollow carbon nanofibers) anode exhibits a capacity of 323 mA h g^{-1} at 0.5 A g^{-1} (50°C) [55], and C-NTO30 (C-containing $Na_2Ti_7O_{15}$) anode maintains the stable values of 225 mA h g^{-1} at 0.2 A g^{-1} (60°C) [56]. Fig. 4d reveals the rate capability of the KV_3O_8 anode at 60°C. The KV_3O_8 anode delivers specific capacities of 453, 415, 381, 340, 294, and 220 mA h g^{-1} at 0.5, 1.0, 2, 5, 10, and 20 A g^{-1}, respectively. Meanwhile, Fig. S8 illustrates the discharge-charge curves of the KV_3O_8 anode at different rates (60°C). The almost 100% Coulombic efficiency indicates the highly reversible redox reaction of the KV_3O_8 anode. Impressively, when switching back to 0.5 A g^{-1}, the KV_3O_8 anode can still restore a specific capacity of 414 mA h g^{-1} (Fig. 4d). In contrast, the V_2O_5 anode at 60°C exhibits relatively low capacities of 308, 273, 225, 179, 127, and 56 mA h g^{-1} at 0.5, 1, 2, 5, 10, and 20 A g^{-1}, respectively (Fig. S9). As revealed by EIS in Fig. S10, the charge-transfer resistance (R_{ct}) of KV_3O_8 is lower at 60°C compared with that of V_2O_5, implying faster charge-transfer kinetics of the KV_3O_8. Furthermore, at the high rate of 10 A g^{-1}, it shows good stability with almost no capacity fading (Fig. 4e). The KV_3O_8 electrode has a capacity of 311 mA h g^{-1} after 1000 cycles at 60°C, indicating its excellent temperature stability. The large layer spacing of KV_3O_8, which improves sodium-ion diffusion, is primarily responsible for the anode's excellent electrochemical performance.

The reaction kinetics was evaluated using the CV technique from 0.1 to 1.0 mV s^{-1} to more intuitively analyze the origin for the outstanding rate performance of KV_3O_8. The CV curves at various scanning rates at 60°C have a slight shift of the cathodic/anodic peaks with the increase of scan rate, as shown in Fig. 5a, indicating that sodium intercalation/delamination kinetics are closely related. For the cathodic peaks (Peak 3, Peak 4) and the anodic peaks (Peak 1, Peak 2) as shown in Fig. 5b, there is a linear relationship between their peak currents (i_p) and the square root of scanning rate ($v^{1/2}$). This illustrates a typical diffusion-controlled process in KV_3O_8. Thus, the Na^+ ion diffusion coefficient (D_{Na^+}) can be determined using the Randles-Sevcik equation [57]:

$$i_p = (2.65 \times 10^5) n^{3/2} S D_{Na^+}^{1/2} C_{Na^+} v^{1/2}, \quad (1)$$

where S is the contact area between KV_3O_8 and electrolyte and n is the charge-transfer number. C_{Na^+} is the concentration of Na^+ in KV_3O_8. According to the slope in Fig. 5b, the D_{Na^+} was cal-

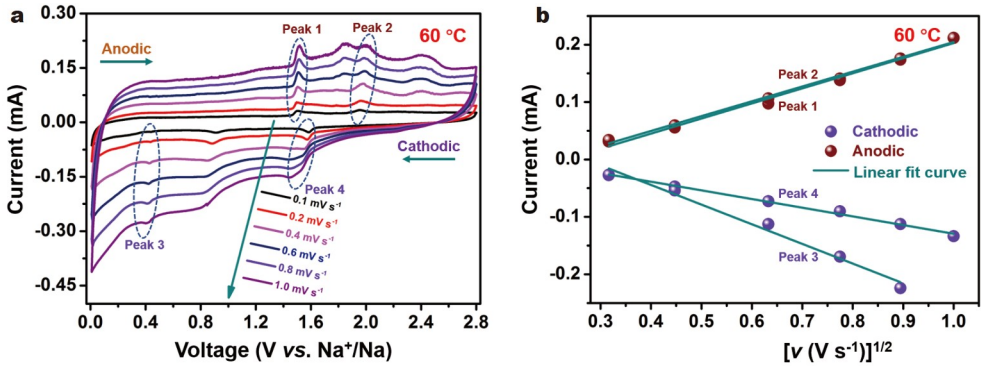

Figure 5 Kinetic analysis of KV_3O_8. (a) CV curves of the KV_3O_8 anode. (b) Relationship between the corresponding peak currents and the square root of scanning rates.

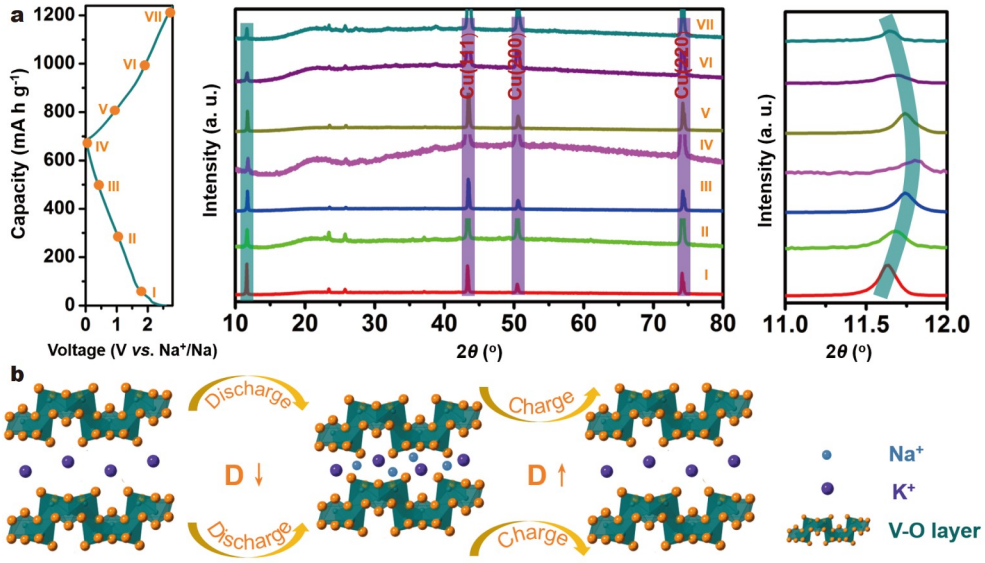

Figure 6 Post-mortem analysis of the KV_3O_8 anode. (a) *Ex-situ* XRD patterns at different discharged/charged states. (b) Interlayer space change of KV_3O_8 in different charge and discharge stages.

culated to be 6.2×10^{-7}–1.9×10^{-9} $cm^2 s^{-1}$ at 60°C.

To reveal the sodium storage mechanism in the KV_3O_8 nanobelts, *ex-situ* XRD measurements were conducted. Fig. 6a shows *ex-situ* XRD patterns during the first discharge/charge cycle, in which no peak appears or disappears during the cycling process, indicating that KV_3O_8 undergoes the reversible intercalation reaction. The amplified view of the *ex-situ* XRD result of KV_3O_8 between 11° and 12° shows that the main peak (100) at 11.7° obviously shifts, which relates to the variation of layer spacing. The peak (100) moves to the highest angle when discharged to 0.01 V, implying a shrinkage of the interlayer spacing, which could be due to the coordination between the oxygen and intercalated Na^+. This unusual phenomenon is frequently observed in layer vanadium oxide materials. After the charging process, this peak shifts completely back to its original position, indicating the high reversibility of the KV_3O_8 anode, which brings the excellent cycling stability. These series of changes during the charge/discharge process are illustrated in Fig. 6b. Based on the results of *ex-situ* XRD, the KV_3O_8 electrode possesses a good reversible Na^+ intercalation/deintercalation performance, guaranteeing excellent cyclability at high temperatures. Fig. S11 illustrates SEM observation of the cycled KV_3O_8 anode. After the 500th and 1000th cycles at 10 $A g^{-1}$, the nanobelts structure of the KV_3O_8 anode can still be well maintained, further proving their excellent stability.

CONCLUSIONS

In summary, KV_3O_8 nanobelts were successfully fabricated using a simple potassium intercalation process for applications in high-temperature SIBs. At 60°C, the KV_3O_8 nanobelt anode possesses a high capacity (414 mA h g^{-1} at 0.1 A g^{-1}), satisfactory rate capability (220 mA h g^{-1} at 20.0 A g^{-1}), and outstanding cycling stability. The satisfactory electrochemical performance of KV_3O_8 can be ascribed to the high Na^+ ion diffusion coefficient (6.2×10^{-7}–1.9×10^{-9} $cm^2 s^{-1}$) and the reversible sodiation/desodiation throughout the entire operating voltage range. Overall, the KV_3O_8 nanobelt is believed to be a promising electrode material to achieve high-performance SIBs for large-scale applications at high temperatures.

Received 25 June 2021; accepted 27 August 2021; published online 30 September 2021

1 Zhao Y, Guo J. Development of flexible Li-ion batteries for flexible electronics. InfoMat, 2020, 2: 866–878

2 Lv T, Zou Z, Li Y, *et al.* Hydrothermal synthesis of high specific capacity Al/Na co-doped V_6O_{13} cathode material for lithium-ion battery. J Electroanal Chem, 2018, 829: 42–50
3 Oh W, Park H, Jin BS, *et al.* Understanding the structural phase transitions in lithium vanadium phosphate cathodes for lithium-ion batteries. J Mater Chem A, 2020, 8: 10331–10336
4 Yang W, Chen D, She Y, *et al.* Rational design of vanadium chalcogenides for sodium-ion batteries. J Power Sources, 2020, 478: 228769
5 Tao L, Yang Y, Wang H, *et al.* Sulfur-nitrogen rich carbon as stable high capacity potassium ion battery anode: Performance and storage mechanisms. Energy Storage Mater, 2020, 27: 212–225
6 Kim PJ, Kim K, Pol VG. A comparative study of cellulose derived structured carbons on the electrochemical behavior of lithium metal-based batteries. Energy Storage Mater, 2019, 19: 179–185
7 Yang J, Li D, Wang X, *et al.* Constructing micro-nano $Na_3V_2(PO_4)_3$/C architecture for practical high-loading electrode fabrication as superior-rate and ultralong-life sodium ion battery cathode. Energy Storage Mater, 2020, 24: 694–699
8 Yang Y, Tang Y, Liang S, *et al.* Transition metal ion-preintercalated V_2O_5 as high-performance aqueous zinc-ion battery cathode with broad temperature adaptability. Nano Energy, 2019, 61: 617–625
9 Zhou X, Yu L, Lou XWD. Nanowire-templated formation of SnO_2/carbon nanotubes with enhanced lithium storage properties. Nanoscale, 2016, 8: 8384–8389
10 Zhang XD, Yue FS, Liang JY, *et al.* Structure design of cathode electrodes for solid-state batteries: Challenges and progress. Small Struct, 2020, 1: 2000042
11 Chae MS, Chakraborty A, Kunnikuruvan S, *et al.* Vacancy-driven high rate capabilities in calcium-doped $Na_{0.4}MnO_2$ cathodes for aqueous sodium-ion batteries. Adv Energy Mater, 2020, 10: 2002077
12 Xu L, Li J, Li Y, *et al.* Nitrogen-doped carbon coated $Na_3V_2(PO_4)_3$ with superior sodium storage capability. Chem Res Chin Univ, 2020, 36: 459–466
13 Wu F, Jiang Y, Ye Z, *et al.* A 3D flower-like VO_2/MXene hybrid architecture with superior anode performance for sodium ion batteries. J Mater Chem A, 2019, 7: 1315–1322
14 Lin B, Zhu X, Fang L, *et al.* Birnessite nanosheet arrays with high K content as a high-capacity and ultrastable cathode for K-ion batteries. Adv Mater, 2019, 31: 1900060
15 Liu Y, Sun Z, Sun X, *et al.* Construction of hierarchical nanotubes assembled from ultrathin V_3S_4@C nanosheets towards alkali-ion batteries with ion-dependent electrochemical mechanisms. Angew Chem Int Ed, 2020, 59: 2473–2482
16 Shen L, Wang Y, Wu F, *et al.* Hierarchical metal sulfide/carbon spheres: A generalized synthesis and high sodium-storage performance. Angew Chem Int Ed, 2019, 58: 7238–7243
17 Ge X, Liu S, Qiao M, *et al.* Enabling superior electrochemical properties for highly efficient potassium storage by impregnating ultrafine Sb nanocrystals within nanochannel-containing carbon nanofibers. Angew Chem Int Ed, 2019, 58: 14578–14583
18 Weng W, Xu J, Lai C, *et al.* Uniform yolk-shell Fe_7S_8@C nanoboxes as a general host material for the efficient storage of alkali metal ions. J Alloys Compd, 2020, 817: 152732
19 Zhang X, Chen D, Zhou Y, *et al.* Mesoporous carbon nanosheet-assembled flowers towards superior potassium storage. Chin Chem Lett, 2021, 32: 1161–1164
20 Fang W, Jiang R, Zheng H, *et al.* Stable sodium metal anode enhanced by advanced electrolytes with SbF_3 additive. Rare Met, 2021, 40: 433–439
21 Zhang W, Li H, Zhang Z, *et al.* Full activation of Mn^{4+}/Mn^{3+} redox in $Na_4MnCr(PO_4)_3$ as a high-voltage and high-rate cathode material for sodium-ion batteries. Small, 2020, 16: 2001524
22 Hu L, He L, Wang X, *et al.* MnSe embedded in carbon nanofibers as advanced anode material for sodium ion batteries. Nanotechnology, 2020, 31: 335402
23 Ding S, Zhou B, Chen C, *et al.* Three-dimensional self-assembled hairball-like VS_4 as high-capacity anodes for sodium-ion batteries. Nano-Micro Lett, 2020, 12: 39
24 Wang J, Luo N, Wu J, *et al.* Hierarchical spheres constructed by ultrathin VS_2 nanosheets for sodium-ion batteries. J Mater Chem A, 2019, 7: 3691–3696
25 Xiao Y, Su D, Wang X, *et al.* CuS microspheres with tunable interlayer space and micropore as a high-rate and long-life anode for sodium-ion batteries. Adv Energy Mater, 2018, 8: 1800930
26 Zhao C, Lu Y, Chen L, *et al.* Flexible Na batteries. InfoMat, 2019, 2: 126–138
27 Zhang Z, Du Y, Wang QC, *et al.* A yolk-shell-structured $FePO_4$ cathode for high-rate and long-cycling sodium-ion batteries. Angew Chem Int Ed, 2020, 59: 17504–17510
28 Zhou P, Sheng J, Gao C, *et al.* Synthesis of $V_2O_5/Fe_2V_4O_{13}$ nanocomposite materials using *in situ* phase separation and the electrochemical performance for sodium storage. Acta Phys-Chim Sin, 2020, 36: 1906046
29 Chen D, Yang W, Jiang Y, *et al.* Fast and reversible Na intercalation in nsutite-type VO_2 hierarchitectures. Adv Mater Interfaces, 2021, 8: 2100191
30 Cheng S, Yao K, Zheng K, *et al.* Self-assembled VS_4 hierarchitectures with enhanced capacity and stability for sodium storage. Energy Environ Mater, 2021, eem2.12195
31 Zhou Y, Zhang X, Liu Y, *et al.* A high-temperature Na-ion battery: Boosting the rate capability and cycle life by structure engineering. Small, 2020, 16: 1906669
32 Rui X, Zhang X, Xu S, *et al.* A low-temperature sodium-ion full battery: Superb kinetics and cycling stability. Adv Funct Mater, 2020, 31: 2009458
33 Huang Y, Zhao L, Li L, *et al.* Electrolytes and electrolyte/electrode interfaces in sodium-ion batteries: From scientific research to practical application. Adv Mater, 2019, 31: 1808393
34 Wei X, Wang X, Tan X, *et al.* Nanostructured conversion-type negative electrode materials for low-cost and high-performance sodium-ion batteries. Adv Funct Mater, 2018, 28: 1804458
35 Zheng X, Bommier C, Luo W, *et al.* Sodium metal anodes for room-temperature sodium-ion batteries: Applications, challenges and solutions. Energy Storage Mater, 2019, 16: 6–23
36 Pu X, Wang H, Zhao D, *et al.* Recent progress in rechargeable sodium-ion batteries: Toward high-power applications. Small, 2019, 15: 1805427
37 Komaba S, Murata W, Ishikawa T, *et al.* Electrochemical Na insertion and solid electrolyte interphase for hard-carbon electrodes and application to Na-ion batteries. Adv Funct Mater, 2011, 21: 3859–3867
38 Wang Z, Qie L, Yuan L, *et al.* Functionalized N-doped interconnected carbon nanofibers as an anode material for sodium-ion storage with excellent performance. Curr Alzheimer Resbon, 2013, 55: 328–334
39 Li Y, Yang C, Zheng F, *et al.* Design of TiO_2eC hierarchical tubular heterostructures for high performance potassium ion batteries. Nano Energy, 2019, 59: 582–590
40 Huang Z, Chen Z, Ding S, *et al.* Multi-protection from nanochannels and graphene of SnSb-graphene-carbon composites ensuring high properties for potassium-ion batteries. Solid State Ion, 2018, 324: 267–275
41 Farbod B, Cui K, Kalisvaart WP, *et al.* Anodes for sodium ion batteries based on tin-germanium-antimony alloys. ACS Nano, 2014, 8: 4415–4429
42 Jiang Y, Peng M, Lan J, *et al.* A self-reconstructed (oxy)hydroxide@nanoporous metal phosphide electrode for high-performance rechargeable zinc batteries. J Mater Chem A, 2019, 7: 21069–21078
43 Gu M, Kushima A, Shao Y, *et al.* Probing the failure mechanism of SnO_2 nanowires for sodium-ion batteries. Nano Lett, 2013, 13: 5203–5211
44 Xiong H, Slater MD, Balasubramanian M, *et al.* Amorphous TiO_2 nanotube anode for rechargeable sodium ion batteries. J Phys Chem Lett, 2011, 2: 2560–2565
45 Pan Q, Zheng F, Liu Y, *et al.* $Fe_{1-x}S$@S-doped carbon core-shell heterostructured hollow spheres as highly reversible anode materials for sodium ion batteries. J Mater Chem A, 2019, 7: 20229–20238
46 Ren Z, Wen J, Liu W, *et al.* Rational design of layered SnS_2 on ultralight graphene fiber fabrics as binder-free anodes for enhanced practical capacity of sodium-ion batteries. Nano-Micro Lett, 2019, 11: 66

47 Shen Q, Jiang P, He H, *et al.* Encapsulation of $MoSe_2$ in carbon fibers as anodes for potassium ion batteries and nonaqueous battery-supercapacitor hybrid devices. Nanoscale, 2019, 11: 13511–13520
48 Chao D, Liang P, Chen Z, *et al.* Pseudocapacitive Na-ion storage boosts high rate and areal capacity of self-branched 2D layered metal chalcogenide nanoarrays. ACS Nano, 2016, 10: 10211–10219
49 Tang H, Xiong F, Jiang Y, *et al.* Alkali ions pre-intercalated layered vanadium oxide nanowires for stable magnesium ions storage. Nano Energy, 2019, 58: 347–354
50 Kim HJ, Jo JH, Choi JU, *et al.* KV_3O_8 with a large interlayer as a viable cathode material for zinc-ion batteries. J Power Sources, 2020, 478: 229072
51 Rui X, Tang Y, Malyi OI, *et al.* Ambient dissolution-recrystallization towards large-scale preparation of V_2O_5 nanobelts for high-energy battery applications. Nano Energy, 2016, 22: 583–593
52 Wang W, Wang T, Fan X, *et al.* Freeze-drying-assisted synthesis of mesoporous $CoMoO_4$ nanosheets as anode electrode material for enhanced lithium batteries. Chem Res Chin Univ, 2019, 35: 261–270
53 Li Z, Dong Y, Feng J, *et al.* Controllably enriched oxygen vacancies through polymer assistance in titanium pyrophosphate as a super anode for Na/K-ion batteries. ACS Nano, 2019, 13: 9227–9236
54 Li Q, Jiang K, Li X, *et al.* A high-crystalline $NaV_{1.25}Ti_{0.75}O_4$ anode for wide-temperature sodium-ion battery. Adv Energy Mater, 2018, 8: 1801162
55 Chen Z, Duan H, Xu Z, *et al.* Fast sodium storage with ultralong cycle life for nitrogen doped hollow carbon nanofibers anode at elevated temperature. Adv Mater Interfaces, 2020, 7: 1901922
56 Zou G, Zhang Q, Fernandez C, *et al.* Heterogeneous Ti_3SiC_2@C-containing $Na_2Ti_7O_{15}$ architecture for high-performance sodium storage at elevated temperatures. ACS Nano, 2017, 11: 12219–12229
57 Chen D, Tan H, Rui X, *et al.* Oxyvanite V_3O_5: A new intercalation-type anode for lithium-ion battery. InfoMat, 2019, 1: 251–259

Acknowledgements This work was supported by the National Natural Science Foundation of China (51801030, 51902032, 51802044, 51902062, and 51802043), the Natural Science Foundation of Jiangsu Province (BK20191026), and Guangdong Natural Science Funds for the Distinguished Young Scholar (2019B151502039).

Author contributions Chen D and Cheng Y performed the methodology, formal analysis, investigation and data curation, and wrote the original draft. Pan H and Sun W participated in the investigation. Geng H and Rui X conducted the conceptualization and revised the paper. All authors contributed to the general discussion.

Conflict of interest The authors declare that they have no conflict of interest.

Supplementary information Supporting data are available in the online version of the paper.

Hongbo Geng received his PhD degree from Soochow University in 2017. He is now working as a full professor at Changshu Institute of Technology. His current research interests focus on functional nanomaterials in electrochemical storage.

Xianhong Rui is a professor at Guangdong University of Technology. He received his BSc degree from the University of Jinan in 2007 and MSc degree from the University of Science and Technology of China in 2010. He obtained his PhD degree from the School of Materials Science and Engineering from Nanyang Technological University in 2014. His research interests mainly focus on the design and fabrication of advanced electrode materials for energy conversion and storage.

层状钒酸钾应用于高性能高温钠离子电池

陈栋[1†], 程亚飞[2†], 潘洪革[3,4], 孙文平[3,4], 耿洪波[2*], 芮先宏[1*]

摘要 在大规模储能领域中, 高温钠离子电池(SIBs)受到了广泛关注. 然而, 较低的充放电效率和较差的循环稳定性仍是制约高温钠离子电池发展的主要因素. 因此, 开发性能优异的电极材料是高温钠离子电池发展的关键. 本工作中, 我们通过简单的钾离子插入法制备了KV_3O_8纳米带作为高温钠离子电池的负极材料. 在60°C高温下, KV_3O_8纳米带表现出高的储钠容量(在0.1 A g^{-1}电流密度下, 可逆容量为414 mA h g^{-1})、卓越的倍率性能(在20 A g^{-1}的高电流密度下为220 mA h g^{-1})和优异的循环稳定性(10 A g^{-1}的电流密度下循环1000次, 容量几乎没有衰减). 此外, 通过非原位XRD分析发现, KV_3O_8纳米带的结构在整个充放电过程中未发生明显变化, 进一步证实了其优异的稳定性. 本研究表明KV_3O_8纳米带具有成为高温钠离子电池负极材料的潜力.

